Dynamics of Single Hydrogen Bubbles at Pt Microelectrodes in Microgravity

Bashkatov, A.; Yang, X.; Mutschke, G.; Fritzsche, B.; Hossain, S. S.; Eckert, K.;

Originally published:

April 2021

Physical Chemistry Chemical Physics 23(2021), 11818-11830

DOI: https://doi.org/10.1039/D1CP00978H

PCCP

ARTICLE TYPE

Cite this: DOI: 00.0000/xxxxxxxxxx

Dynamics of Single Hydrogen Bubbles at Pt Microelectrodes in Microgravity†

Aleksandr Bashkatov*[a], Xuegeng Yang[a], Gerd Mutschke[a], Barbara Fritzsche[ab], Syed Sahil Hossain[a] and Kerstin Eckert*[ab]

Received Date
Accepted Date

DOI: 00.0000/xxxxxxxxxx

The dynamics of single hydrogen bubbles electrogenerated in acidic electrolytes at a Pt microelectrode under potentiostatic conditions is investigated in microgravity during parabolic flights. Three bubble evolution scenarios have been identified depending on the electric potential applied and the acid concentration. The dominant scenario, characterized by lateral detachment of the grown bubble, is studied in detail. For that purpose, the evolution of the bubble radius, electric current and bubble trajectories, as well as the bubble lifetime are comprehensively addressed for different potentials and electrolyte concentrations. We focus particularly on analyzing bubble-bubble coalescence events which are responsible for reversals of the direction of bubble motion. Finally, as parabolic flights also permit hypergravity conditions, a detailed comparison of the characteristic bubble phenomena at various levels of gravity is drawn.

Broader context

Hydrogen gas is a prominent energy source of high practical relevance in energy storage via power-to-gas processes. The gas is widely involved in numerous applications as a secondary or desirable product of the process. One example is the production of oxygen in the International Space Station by water electrolysis, where the hydrogen plays a secondary role, but could be used for the water recovery via the Sabatier reaction. The gas bubbles occupy the electrode surface, reducing the rate of electrochemical reaction and the efficiency of the system. Therefore, similarly to water electrolysis on the ground, both hydrogen and oxygen gas bubbles need to be removed in microgravity. The bubble evolution and departure become especially challenging in the absence of buoyancy and require intensive research at both macro- and micro-scales. The present study provides a detailed overview of the evolution and detachment of a single hydrogen bubble in the microgravity environment within various experimental parameters. It aims to advance the future design of water electrolysis and photoelectrochemical water splitting experiments, and in a more general sense to develop strategies for increasing the gas production rate in microgravity applications.

[a] *Institute of Fluid Dynamics, Helmholtz-Zentrum Dresden-Rossendorf, Bautzner Landstrasse 400, Dresden, 01328 Germany; E-mail: a.bashkatov@hzdr.de*

[b] *Institute of Process Engineering and Environmental Technology, Technische Universität Dresden, Dresden, 01062 Germany; E-mail: k.eckert@hzdr.de*

† Electronic Supplementary Information (ESI) available: [details of any supplementary information available should be included here]. See DOI: 00.0000/00000000.

1 Introduction

Electrolytic gas evolution is a complex phenomenon which involves several fields of science, such as electrochemistry, surface and interface physics/chemistry and fluid dynamics, at length scales ranging from nanometers to centimeters[1,2]. Until recently, details of the process, such as the bubble departure, have not been understood in depth[3–5]. It is only in the last few years that a better understanding of balance of forces acting on the bubble has been achieved, as the thermal Marangoni and electric forces caused by charge absorption, which had not been considered before, have been uncovered and quantified[6–8].

On the other hand, electrolytic gas evolution is a basic part of important technologies such as alkaline water electrolysis, which has gained further importance in light of worldwide efforts to decarbonize the energy system[9,10]. A better knowledge of how to further advance the bubble departure could reduce energy losses and thus make green hydrogen cheaper. In addition, hydrogen also plays an important role in space technologies. Apart from propulsion applications, hydrogen appears as a by-product when electrolytically producing oxygen for life support on spacecraft such as the International Space Station (ISS). Beside the aspect of energy efficiency, advanced concepts also exist to utilize the hydrogen produced. By feeding a Sabatier reaction, water can be gained in space, as described in the In-Situ Resource Utilization (ISRU) concept[11].

The process of electrolytic gas evolution is strongly influenced by gravity, as the force balance influences the moment when the attached bubble departs from the electrode[12,13]. At high current

densities, which are relevant to industrial applications, the bubble evolution is quite fast and therefore difficult to study experimentally. Here, microgravity offers the opportunity to slow down the bubble departure and to grow larger bubbles, making it possible to study the processes involved more accurately. Moreover, as the force balance on the bubble is modified, the bubble dynamics might uncover effects which cannot be observed in standard gravity.

The first experiments to study hydrogen bubble dynamics in microgravity were performed during the TEXUS 1 program (sounding rocket) in 1978 [14,15]. Although some of the results reported were questioned in later works, e.g. with respect to the departure size of the bubbles, these pioneering works inspired intense further research. The dynamics of multiple hydrogen and oxygen bubbles on a plane electrode were studied at drop towers [16–22], during parabolic flights [23,24], on a sounding rocket [14] and at the space station [25]. As additional complexity arises from the interaction of the bubbles during growth, investigations into single hydrogen and oxygen bubbles grown on a microelectrode were later also started by Matsushima et al. [26] and Sakuma et al. [27]. The importance of bubble-bubble interaction with respect to the surface tension force on a micro-pin-finned electrode was discussed in Zhou et al. [28].

As buoyancy is considerably reduced in microgravity, the bubbles stay longer and grow larger at the electrode compared to terrestrial conditions [18,19,23,25]. Further forces come into play. Already in 1982 thermocapillary effects were suspected to affect the motion of small oxygen bubbles growing at a microelectrode [29]. Meanwhile, strong evidence exists that thermocapillary effects caused by temperature gradients along the bubble interface lead to mutual attraction of neighboring hydrogen bubbles growing at an electrode [30] and also to electrode-normal force components which affect the bubble departure [7,8,31]. In electrolysis, the temperature gradients arise naturally from reaction overpotentials at the electrodes and spatially inhomogeneous ohmic losses in the electrolyte. In addition to the thermocapillary effect, Lubetkin was the first to discuss the possible influence of solutocapillary effects caused by the adsorption of ions or molecules at the bubble interface which modify the surface tension as well [32,33]. However, for the case of hydrogen bubbles growing on a microelectrode it could be clearly shown that the thermocapillary effect dominates and is mainly responsible for the vortical electrolyte flow observed near the bubble [7]. The thermocapillary Marangoni force is given by the integration of the thermocapillary stress over the interface,

$$F_M = -\int \tau_M dA$$

where $\tau_M = (\partial\gamma/\partial T)(\partial T/\partial s)$ is due to the variation of interfacial tension γ with temperature T along a length s at the interface. The total force on the bubble resulting from the thermocapillary effect is obtained from the integration over the full stress tensor, thereby additionally accounting for surface-normal stress components including pressure [34].

A second force, already mentioned above, is the electric force

$$F_e = \int \sigma E dA\,,$$

which the hydrogen bubble carrying a surface charge density σ, experiences in the electric field $\mathbf{E}$ between the anode and cathode. When assuming a uniform surface charge density on the bubble, this electric force varies non-linearly with the bubble position at a microelectrode, governing the oscillations in the vertical bubble positions observed in Bashkatov et al. [6].

Furthermore, and especially in alkaline electrolytes, the detachment of individual bubbles from the electrode in microgravity is triggered by inertia caused by bubble collisions or bubble coalescence [17–19,25]. The coalescence behavior of bubbles is known to be influenced by the pH value and specific ion effects of the electrolyte under study [35]. Hydrogen bubbles coalesce more easily in acidic H_2SO_4 than in alkaline KOH solutions [18,19]. As this holds true regardless of the gravity level, surface chemistry plays a major role here. The wettability of plane and modified surfaces with respect to hydrogen and oxygen in microgravity conditions was studied by Brinkert et al. [16] and Sakuma et al. [20,27]. The existence of a carpet of microbubbles covering the microelectrode, above which the hydrogen bubbles evolve in an acidic electrolyte, is known from previous work [6]. However, the detailed impact which the coalescence events between the carpet and main bubble exert on the dynamics remains unresolved.

This work provides a systematic study of hydrogen bubble dynamics on a microelectrode in an acidic electrolyte under microgravity conditions. Three characteristic scenarios of the bubble evolution are unveilled, and a key feature of the bubble under microgravity, namely the slow lateral bubble motion prior to bubble departure, is studied in detail. We show that coalescence events play a significant role in the bubble evolution and may cause sudden reversals within the lateral bubble motion or cause the bubble to jump away from the electrode. Finally, the availability of both micro- and hyper-gravity conditions on parabolic flights enables a detailed comparison to be drawn of the characteristic bubble phenomena at various levels of gravity.

2 Experimental design

Several platforms are available to perform experiments in a microgravity environment. They differ in terms of the residual fraction of g, which varies from $10^{-2}g$ in parabolic flights to $10^{-6}g$ in a drop tower or on the ISS. The possibility to control an experiment on-board in person, the relatively long microgravity duration, and the comparatively short preparation time at manageable costs make parabolic flights attractive and competitive. However, the quality of microgravity, henceforth abbreviated to micro-g or μg, is limited in comparison to drop tower and ISS experiments.

The microgravity experiments of this work were performed during the *34th DLR Parabolic Flight Campaign* in September 2019, conducted by the company Novespace. The campaign lasted for two days, with 31 parabolas daily. Figure 1(a) offers a schematic diagram of the aircraft altitude (black line) reflecting its trajectory, and the corresponding gravitational acceleration g (red line). Each parabolic maneuver lasts for about 3 minutes, cf. Fig. 1a. It includes a micro-g phase ($\sim 10^{-2}g$ for about 22 s) sandwiched by two hyper-g phases ($\sim$1.5...1.8g for about 20 s) depending on both the velocity and the aircraft pitch angle, referring to the angle between the fuselage and the ground. Micro-g is

achieved in the free-fall phase of the airbus at a pitch angle range $\sim 47°...0...-42°$. The term residual buoyancy refers to buoyancy caused by residual gravitational acceleration, abbreviated by g_{res}. g_{res} is determined as

$$g_{res} = \sqrt{g_{res,x}^2 + g_{res,y}^2 + g_{res,z}^2},$$

where $g_{res,x}$, $g_{res,y}$ and $g_{res,z}$ are the components of residual gravitational acceleration in x-, y- and z- directions, measured during the flight by the aircraft crew.

The experiments require a comprehensive setup design in terms of both safety and robustness. In accordance with Novespace's safety regulations, all liquid-containing cells were sealed and mounted on a breadboard inside a watertight Zarges ® box to fulfill the required double-stage protection principle. Furthermore, liquid-adsorbing material was placed across the breadboard. Parts of the setup are represented in Fig. 1b-c.

The experimental setup to perform the electrolysis is similar to Yang et al.[3], cf. Figure 1c. It comprises three electrodes inserted into the glass cuvette of 10 × 10 × 40 mm^3 and filled with the electrolyte. The hydrogen bubbles were evolved on a ⌀100 μm Pt microelectrode — cathode, installed horizontally from the bottom of the cuvette. Two ⌀0.5 mm Pt wires installed from the top were used as the anode and pseudo reference electrode. The electrolysis was carried out in an acidic electrolyte H_2SO_4 with different concentrations of 0.02, 0.1 and 0.5 mol/L, and was controlled by an electrochemical station (Autolab) in potentiostatic mode within a potential range of -1.2...-8 V for 70 s. To prevent any leakage, the electrochemical setup was fixed inside an outer housing by four M4 screws, reliably sealed from the top using the O-ring. The housing has two optically accessible observation windows. The holes through which the cathode, anode and reference electrode were inserted were sealed with nail polish. Three such housings, filled with different electrolytes, formed a cell system to be studied on the day of the flight. The cell system was mounted on a motorized linear stage (LIMES, OWIS GmbH). After the aircraft took off, each of the housings were deliberately opened and consequently closed, to equilibrate the pressure inside (1 atm) with that in the cabin (0.8 atm).

To study the bubble dynamics in this cell system, microscopic shadowgraphy (50 frames per second, spatial resolution 678 pix/mm) coupled to electrical current measurements (sampling rates from 0.4 to 1 kHz) were simultaneously performed. The shadowgraph systems employs a microscope connected to a high-speed camera (IDT, NX4-S1) and a back-light to illuminate the cell system, see Figure 1b. To avoid problems caused by vibrations of the aircraft, the microscope system (Thalheim Spezialoptik, Germany) has been designed without any springs. The motorized linear stage permits the horizontal movement of the cell system between groups of parabolas to image the bubble evolution at different electrolyte concentrations. Since the linear stage is aligned parallel to the axis of the aircraft while the camera is directed perpendicularly to it, the impact of pitch angle variation can be traced in the image plane observed. The influence of this effect is depicted again in a magnified diagram in Figure 1d, showing the positively charged hydrogen bubble floating above the cathode inclined by the pitch angle (negative here). Since the camera and cell system are rigidly fixed on the breadboard/aircraft, an inclination due to pitch angle variation is not visible in the images displayed later. In general, the bubbles remain in the focus plane of the optics, which allows the accurate measurement of radius and position of the bubbles over time from analysing the acquired images by a Matlab R2019b algorithm (for details see the Supplemental Material of Bashkatov et al.[6]). In rare cases, when the bubble moves out of focus, the electric current is used instead. By integrating the electric current I over time t, according to Faraday's law, the total charge

$$Q = \int I(t)dt$$

and the hydrogen volume produced can be calculated, and finally converted to the bubble radius R (for details see Yang et al.[3]).

The lines of the electric current density j flowing between the anode and cathode are schematically drawn in Figure 1d. They bend around the non-conducting hydrogen bubble with a radius R. The coordinate system originates at the center of the cathode and the x-axis is directed to the rear part of the aircraft. A relevant quantity in the later analyses is the difference between the x-positions of the bubble and electrode centers, X, which is positive when the bubble moves to the right and negative when it moves to the left.

3 Experimental results and discussion

3.1 Scenarios of single bubble evolution in microgravity

The H_2 bubble evolution on a microelectrode under microgravity was found to follow three scenarios: (1) - *growth and lateral detachment*, (2) - *continuous growth* or (3) - *initial growth and stagnation*. Figure 2 gives an example case for each scenario based on the electric current (I) flowing between the cathode and anode, versus time. The results shown for (1), (2) and (3) were achieved in sulfuric acid H_2SO_4 with a concentration of 0.02 mol/L at -5 V, 0.1 mol/L at -3 V and 0.5 mol/L at -3 V, respectively.

In Scenario (1), the upper plot in Fig. 2, numerous perturbations in the current are visible. They result from multiple bubble evolution cycles, i.e. nucleation-growth-detachment events, during the μg phase of one parabola. The newly nucleated bubble increases the Ohmic resistance and thus decreases the current. Thus, the cathodic current increases when the bubble detaches. Detachment events, marked by red circles, are caused mainly by the combination of varying pitch angle, residual buoyancy and coalescence. Scenarios (2) and (3) are particular, less frequent cases. Scenario (2) is characterized by the bubble occasionally sticking to the glass/electrode interface with partial coverage of the electrode area and continuous slow growth during microgravity. Scenario (3) involves almost the entire electrode area being blocked by the hydrogen bubble for most of its growth period. As a result, the current falls to a value close to zero.

The number of hydrogen bubbles successfully recorded and processed during the parabolas of the *34th DLR Parabolic Flight Campaign* is represented in Table 1 for each scenario. They are grouped according to the cathodic potential and electrolyte concentration used. In Scenario (1) up to 17 bubbles were released

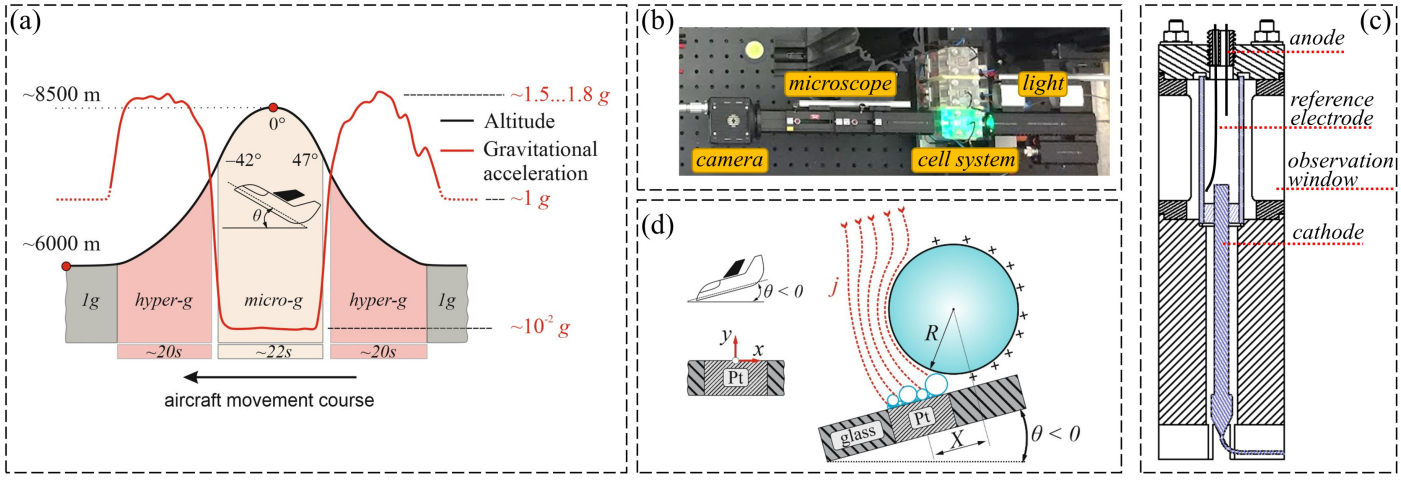

Fig. 1 (a) Schematic representation of a parabola trajectory of the aircraft coupled with gravitational acceleration zones (not to scale). The black line represents the aircraft altitude and the red line the component of the gravitational acceleration that is directed normal to the aircraft. θ denotes the pitch angle varying over time. (b) The experimental setup comprising the camera, microscope, backlight and cell system mounted on the breadboard. (c) The scheme of the housing comprising the three-electrode electrochemical setup i.e. anode, cathode, reference electrode and glass cuvette. (d) Schematic representation of the positively charged bubble above the cathode when the aircraft is at pitch angle θ. R and X denote the bubble radius and the lateral (x) bubble position (see the coordinate system) with respect the electrode center. The red dotted lines sketch the path of the electrical current j towards the cathode.

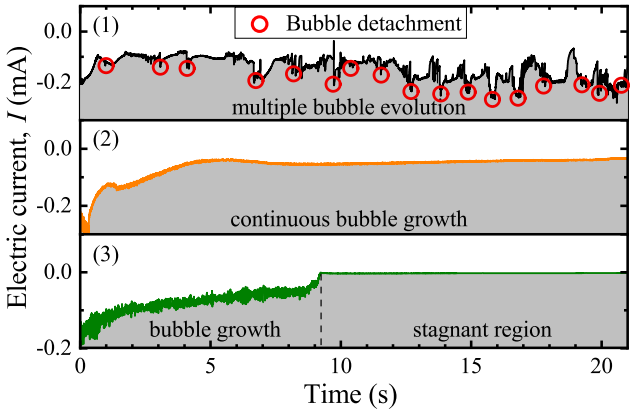

Fig. 2 The three scenarios of bubble evolution observed in microgravity: (1) - *growth and lateral detachment* (0.02 mol/L H_2SO_4 at -5 V), (2) - *continuous growth* (0.1 mol/L at -3 V) and (3) - *initial growth and stagnation* (0.5 mol/L at -3 V).

in μg within one parabola, e.g. in 0.02 mol/L at -5 V, while the evolution of a bubble takes as long as a whole μg phase in Scenarios (2) and (3). Thus, contrary to expectations, Scenario (1) and not (2) or (3) is by far the most dominating scenario. This implies that the statistics behind the bubble ensembles are naturally elaborated in more detail for Scenario (1) compared to (2) and (3).

In Scenario (3), the initial fluctuations are caused by weak horizontal bubble vibrations which occur during growth in terrestrial conditions as well.

In the following, we focus entirely on Scenario (1) in the shaded area of Table 1. Based on the significant number of detected H_2 bubbles, systematic features of the bubble dynamics under microgravity can be extracted.

3.2 Scenario (1) - Growth and lateral detachment

3.2.1 Phenomenology

Figure 3(a) shows an example of a bubble evolution for 0.02 mol/L at -5 V. The set of images tracks the temporal evolution of a selected bubble (marked by a red circle) and its motion relative to the electrode. After just a short time $\mathcal{O}$(ms), see the first image at 0.02 s, a single hydrogen bubble is visible on the microelectrode. The further bubble growth is mainly governed by continuous coalescence with newly nucleated bubbles on a time scale $\mathcal{O}(\mu s)$. Every coalescence event shifts the bubble position slightly (see below). As a result, the mother bubble frequently levitates by several μm above the electrode. With progressing time during the parabola, the residual buoyancy,

$$f_{b,\mu g} = \frac{4}{3}\pi R^3 \rho_l g_{res},$$

forces the marked bubble to move to the right side away from the electrode until it finally departs (here at 1.10 s). g_{res} refers to the residual gravitational acceleration plotted in Fig. 4a. ρ_l is the density of the electrolyte.

This *lateral detachment* under the μg condition of the parabolic flight is one of the main differences to terrestrial experiments where vertical detachment occurs due to the much higher buoyancy,

$$f_{b,1g} = \frac{g}{g_{res}} f_{b,\mu g}.$$

The direction of bubble movement is governed by the residual gravitational acceleration g_{res}, which is related to the aircraft pitch angle θ, referring to the angle between the fuselage and the horizon (cf. Fig. 1). For pitch angles larger than zero, the bubble thus travels in the direction of the cockpit; otherwise, it travels in the opposite direction. As the bubble moves away from the electrode center, it passes through several of the nucleation

Scenario (#)	Potential (V)										H_2SO_4
	-1.2	-1.5	-1.8	-2	-3	-4	-5	-6	-7	-8	(mol/L)
							17	12	9	7	0.02
(1)	4	10	1		1						0.1
	7	10	8	11	2	3	1	1			0.5
(2)				2	1	1	1		1		0.1
		1	1	1	3	2	1				0.5
(3)					1	2	1	1			0.5

Table 1 Number of bubble studies performed at different potential and concentration.

sites of the microelectrode. As a result, some of the small bubbles formed there merge directly with the main bubble, while others coalesce to form another microbubble to one side (examples are at 0.76 s or 0.90 s). Because the lateral velocity of the mother bubble is low, the second smaller bubble (t = 0.90 s) has enough time to expand and to coalesce with it. We use the term "mother bubble" throughout this work for the dominating and biggest bubble at the electrode, which continuously grows mainly by consuming smaller bubbles. Thus, we distinguish between the primary, mother bubble growing on the electrode and the continuously forming bubble swarm at the electrode. The evolution of the mother bubble, which has a substantially longer lifetime and bigger detachment diameter than the smaller bubbles, is tracked over time and is the main target of the present analyses.

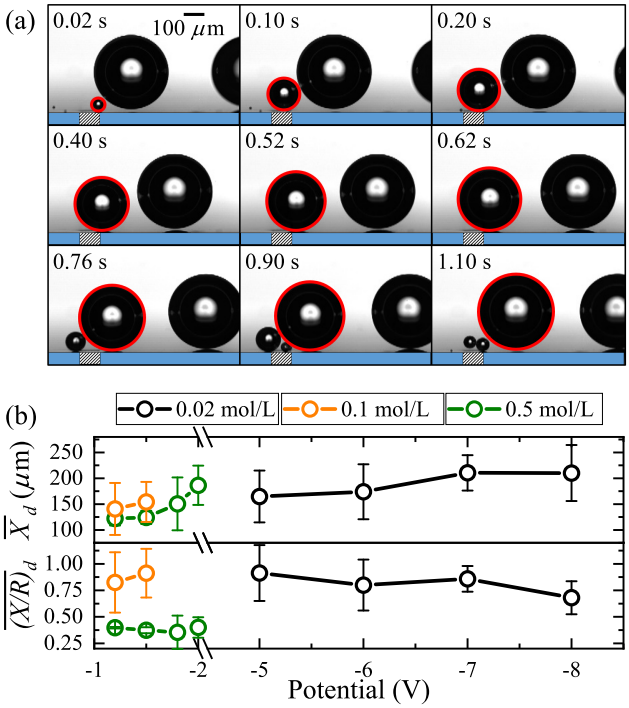

Fig. 3 (a) Examples of bubble evolution in micro-g recorded at 50 frames per second in 0.02 mol/L at -5 V. The target bubble is circled in red. The hatched area is the Pt electrode, while the blue region is the glass bottom. (b) The averaged detachment distance $\overline{X}_d$ between the electrode and bubble centers (upper plot) and $\overline{(X/R)}_d$ normalized with the bubble radius R_d (bottom plot) versus potential for different electrolyte concentrations.

The detachment of the mother bubble is defined as that moment at which the last coalescence with newly appearing bubbles occurs. Thus it is the moment when the detaching bubble interacts for the last time with younger bubbles. This definition of the detachment event, which is later correlated with the electric current, makes sense when focusing on a small electrode area only. At large planar electrodes, where several large bubbles may detach in parallel, the definition needs to be modified. At the instant of detachment, the bubble reaches the maximum lateral distance, X_d, from the electrode center, where interaction with the electrode vanishes. The bubble ceases to coalesce and leaves the electrode at its detachment diameter. Figure 3(b) presents the departure distance $\overline{X}_d$ versus potential at different electrolyte concentrations. In the following, unless noted otherwise, the bar over the symbol denotes averaging over all bubble cycles available at a given voltage and concentration. The margins given in the data refer to the standard deviation. To give an estimate, $\overline{X}_{d,all}$ averaged over all observed cases is (168 ± 50) μm. It is instructive to relate $\overline{(X)}_d$ to the bubble radius: we note a close similarity in that $\overline{(X/R)}_d \sim 0.8$ at small concentrations (0.02 and 0.1 mol/L) while a reduction to $\overline{(X/R)}_d \sim 0.4$ is found at the larger concentration 0.5 mol/L. Thus the bubbles already detach at a smaller lateral distance from the electrode center at higher concentrations.

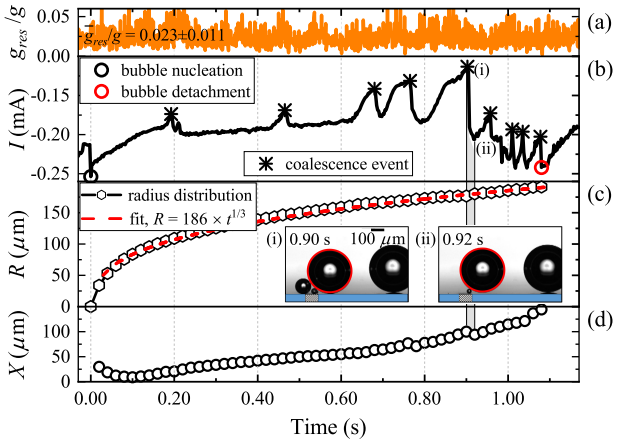

Fig. 4 (a) Residual gravitational acceleration g_{res}. (b) Electric current I. (c) Bubble radius R (black line with diamond symbols). The two insets show the bubble before and after coalescence. The target bubble is circled in red. The red dashed line is a fit to the experimental data, $R \propto t^{1/3}$. (d) Bubble center position relative to the electrode center X. All data correspond to the bubble evolution of Fig. 3(a) (0.02 mol/L at -5 V).

To analyze the bubble evolution shown in Fig. 3 in more de-

tail, in Figure 4 we plot the electric current I (b), the bubble radius R (c) and the lateral displacement X (d) versus time simultaneously with the characteristic residual gravitational acceleration $\overline{g_{res}} = (0.023 \pm 0.011)g$ (a). The electric current, captured with a temporal resolution of 400 Hz, reflects the bubble dynamics, which starts with the nucleation (black circle) and ends with the detachment (red circle). In between, numerous coalescence events occur, marked by black stars. Two inset images (i) and (ii) in Figure 4c show the target bubble immediately before and after its coalescence with smaller microbubbles. They document the correlation in time between coalescence and jumps in the electric current, see the time slot marked in gray. Indeed, every minimum in the electric current can be assigned to a coalescence event. After coalescence, both a jump-like increase in the electric current amplitude and a jump by the bubble from the surface up for about 5 μm (resolution is about 1.5 μm/pix) are observed, together with a subsequent motion in the reverse direction, see Figure 4d. This motion, which only lasts less than 0.02 s, is analyzed in more detail in Fig. 6.

The radius $R(t)$ and the horizontal bubble position $X(t)$, obtained via image analysis, are plotted versus time in Figure 4c-d. The red dashed line in (c) corresponds to a fit according to $R \propto t^{1/3}$. Thus, in this particular case, the bubble evolution follows the conventional growth law in accordance with Yang et al.[3], Darby et al.[36], Kristof et al.[37]. However, this behavior is not the rule under microgravity, as outlined in the following: The nature of parabolic flight is that the pitch angle (cf. Fig. 1) continuously varies in time, e.g. it changes in the range from 47 to $-42°$ under μg. As a result, the bubble might roll over the electrode, driven by the residual gravity. Thus, the electric current is determined not only by the size of the bubble (which determines the circular area at the electrode that is deactivated by the bubble), but also by the pitch-angle-dependent bubble position.

The carpet of smaller microbubbles mentioned in Section 1, which levitates the mother bubble in terrestrial experiments[6] and in the $1g/1.8g$ experiments in this campaign, is either much thinner under micro-g, and therefore difficult to resolve, or forms beside the receding bubble. These differences are discussed in Section 3.3.

3.2.2 Bubble position and radius versus time

Figure 5 shows the lateral position (a) and the bubble radius (b) for five representative bubbles over time for two different parameter combinations: (i) 0.1 mol/L, -1.5 V and (ii) 0.02 mol/L, -6 V. In (i), the lateral movement of the bubble along the electrode proceeds in an orderly manner. The bubble moves towards the left (cockpit) if the pitch angle takes positive values. This is documented by the lines numbered 1 (41°...34°) and 2 (34°...20°). For negative pitch angles, the bubble moves to the right, i.e. towards the rear of the aircraft. The bubbles belonging to lines 4 (1°...-19°) and 5 (-19°...-33°) exhibit this behavior. For pitch angles close to zero (line 3: 20°...1°), the bubble stays at the electrode without lateral movement. Note that the first angle (20°) in the latter case refers to the pitch angle at the start of the bubble evolution, while the last one, here 1°, is that where the line terminates and the bubble detaches from the electrode. Thus, it is obvious that the lifetime increases from the 1^{st} to 3^{rd} lines and decreases from the 3^{rd} to 5^{th} lines as the pitch angle decreases and increases, correspondingly. In case 3, where the pitch angle is closest to zero, the bubble detaches perpendicularly to the electrode surface. A more detailed analysis of the correlation between bubble radius, bubble position, residual gravity and pitch angle for this case can be found in the Supplementary Information†.

By contrast, the lower concentration in (ii) does not show this structured behavior. Moreover, the initial bubble position and lateral movement are spatially scattered among several bubbles and the direction of movement does not always correlate with the pitch angle. The growing bubble is often being pushed aside by the freshly nucleated bubbles with and without subsequent coalescence. This behavior remains similar among other potentials at all the concentrations studied. Events where a fast reversal in the direction of lateral motion occurs, characterized by a change of sign in dX/dt, are marked by black circles. Here, for short instants of time, the bubble moves backwards, towards the electrode center. These events occur much more frequently for the lower concentration (ii) — 0.02 mol/L than compared to (i) — 0.1 mol/L, where they only appear exactly before detachment, and with smaller amplitude. The bubble behavior in 0.5 mol/L (not shown) is similar to 0.1 mol/L and with almost no backward motion events caused by coalescence.

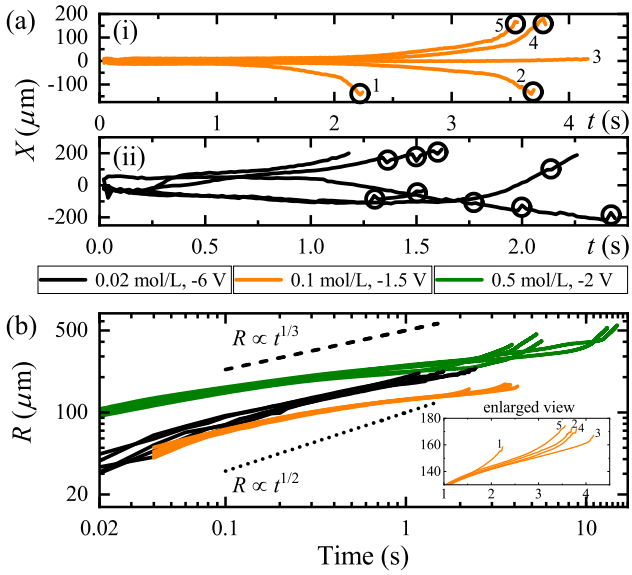

Fig. 5 (a) Bubble position X for multiple bubbles over their lifetime: pitch angle-correlated motion for 0.1 mol/L and -1.5 V (orange line, see main text) and non-correlated case for 0.02 mol/L, -6 V (black line). The black circles in the plots indicate a backward motion of the bubble. (b) Evolution of the radius $R(t)$ for the bubbles shown in (a), supplemented by the case 0.5 mol/L, -2 V (green). The black dashed line refers to the coalescence-driven 1/3-power law and the dotted one to the diffusion-controlled 1/2-power law of bubble growth.

Fig. 5(b) examines the development of the bubble radius over time for the bubbles of (a), complemented by the 0.5 mol/L, -2 V case (green). The bubble evolution starts with a fast growth leading to bubble radii of about 30-40 μm for 0.02 and 0.1 mol/L and 90 μm for 0.5 mol/L just 20 ms after nucleation. Then, a

smoother evolution follows which terminates in a rapid increase in R before detachment. The growth rate, dR/dt, generally depends on the electric current, the magnitude of which might be substantially enhanced while the bubble drifts away from the electrode. The precedence of 0.02 mol/L over the 0.1 mol/L lines is caused by the higher potential which compensates for the difference in electrolyte concentration. As a result, the current is higher, and hence also the growth rate. The inset in Fig. 5(b) displays the individual $R(t)$ dependences corresponding to the bubble trajectories in Fig. 5a. It is obvious that those bubbles which experience a lateral displacement evolve more rapidly than the stagnant bubble no. 3.

The black dashed and dotted lines represent the theoretical 1/3-power-law and 1/2-power-law growth models. The difference between the experiment and theory is visible - the experimental slope changes over time. Since the experiments are conducted in potentiostatic mode, the electric current determining the bubble growth rate depends on the bubble size, and also on its position, which is influenced by the pitch angle. Therefore, the coefficient in the power-law relation changes constantly during the bubble evolution in several series of experiments. However, as shown in Fig. 4(c), the 1/3-power law might fit to the experimental data, when current does not fluctuate much along the evolution.

Microgravity modifies the bubble dynamics known from terrestrial experiments. Contrary to expectations, the bubble growing under μg does not completely block the active area of the electrode (Scenarios (2) and (3)). Instead, the residual gravitational acceleration enables the bubble to move laterally away from the electrode as shown in Figures 4d and 5a. The curves in Fig. 5a demonstrate two important features to be investigated next, namely the backward motion (Section 3.2.3) and the scattering lifetime of the bubbles (Section 3.2.4). Both phenomena seem to be coupled as the bubbles have a higher lifetime (Fig. 5a) if they stay close to the electrode center instead of moving laterally aside, where their growth is affected by more intensive coalescence.

3.2.3 The "backward motion" of bubbles

A representative event of the remarkable backward motion of a bubble is shown in Figure 6(a) for 0.02 mol/L at -8 V. The images depict a bubble which moves laterally from the left to the right (see arrow in Fig. 6a), similarly to Fig. 4d. The bubble motion is accompanied by coalescence with smaller bubbles. As an obvious result of the latter process, the bubble moves for a short timespan in the opposite direction, *backwards*, towards to the electrode center. To further analyze this backward motion, in Fig. 6(b) we plot not only the first derivatives of the radius dR/dt and bubble position dX/dt, but also the electric current I and the bubble position X. Here, the backward motion, corresponding to timespans with $dX/dt < 0$, takes place in the grayed zones of Fig. 6(b). The first backward motion at 2.18...2.36 s is particularly well resolved. However, two further events at 2.60 s and after 2.70 s emphasise that the backward motion is not a singular event. In the following we focus on the first grayed window of this motion. At certain instants of time, Fig. 6(b) around 2.10 s, the bubble decelerates and its velocity, dX/dt, gets close to zero. The vertical red dashed line in Fig. 6(a) serves as a reference for the initial bubble position at $t = 2.18$ s. Between the first and second frames, the mother bubble coalesces with a relatively big secondary bubble. As a result, the mother bubble moves to the left. In a series of continuous coalescence events with smaller bubbles, the mother bubble moves backwards for about 130 μm in 0.18 s until the velocity is zero again.

It is obvious that the sudden change from $dX/dt > 0$ to $dX/dt < 0$, which initializes the backward motion, is accompanied by a rapid increase in both dR/dt and the current I due to coalescence. The bubble velocity and current increase toward a maximum, and drop again later. When the electric current approaches a value similar to that before the backward motion started, the bubble reaches a velocity around zero. This marks the end of the backward-motion phase and the bubble continues to move in the direction set by the pitch angle and buoyancy.

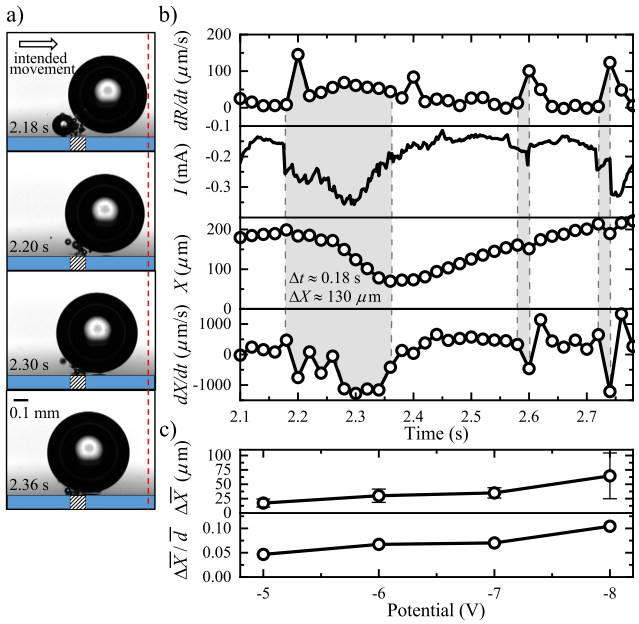

Fig. 6 (a) Image sequence showing the backward motion of the bubble following a coalescence event in 0.02 mol/L at -8 V. (b) First derivative of $R(t)$ and $X(t)$ over time coupled with current response I and bubble position X in 0.02 mol/L at -8 V. (c) Absolute distance $\Delta\overline{X}$ and relative distance $\Delta\overline{X}/\overline{d}$ of the backward motion of bubbles at different potentials in 0.02 mol/L. Each point is an average over 10 return events. The error bars refer to the corresponding standard deviation.

Figure 6(c) shows the mean lateral distance $\Delta\overline{X}$ which the bubbles travel during the backward motion in 0.02 mol/L at a potential range of -5...-8 V. $\Delta\overline{X}$ was obtained by averaging over the ten cases of the largest backward motions ΔX at each potential. The margins show the corresponding standard deviation. The average amplitude $\Delta\overline{X}$ is seen to increase with the potential. The increase is not compensated for if $\Delta\overline{X}$ is related to the mean detachment diameter $\overline{d}$. While the displacement at -5 V is about 5% of the bubble diameter, it is 10% at -8 V.

As the backward motions happen less frequently for 0.1 and 0.5 mol/L compared to 0.02 mol/L, the statistics are not sufficient

to show a similar plot for these concentrations. Coalescence is the main event preceding the backward movement. It might be possible that additional forces, see Section 3.2.5, play a further role.

3.2.4 Detachment diameter and lifetime of bubbles

Figure 7(a) summarizes the behavior of the mean detachment diameter $\overline{d}$ and the mean bubble lifetime $\overline{T}$ versus potential for different concentrations. Let us recall that detachment is defined as the moment of the last coalescence event which a bubble receding from the electrode undergoes with a newly formed one. As expected, both $\overline{d}$ and $\overline{T}$ increase with the potential and the concentration. This is similar to what is found in terrestrial experiments, where higher retarding forces were reported (see next Section)[31]. One exception is the experiments in 0.1 mol/L, where both $\overline{d}$ and $\overline{T}$ remain unchanged between -1.2 V and -1.5 V. This is obviously caused by a substantially smaller electric current in 0.1 mol/L, cf. Fig. 10, despite the higher concentration. As a result, $\overline{d}$ is very close to the value in 0.02 mol/L at -5 V but $\overline{T}$ is larger by a factor of ~ 3.

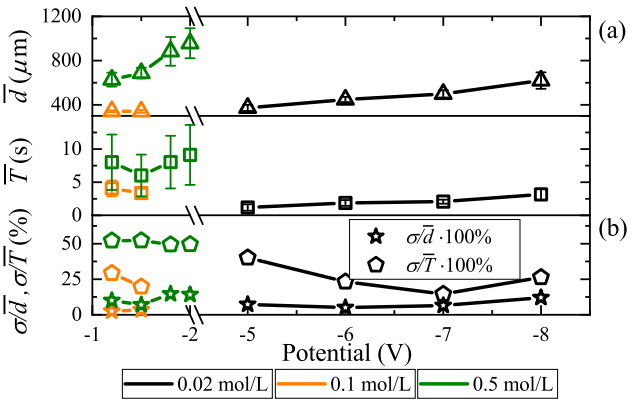

Fig. 7 (a) Bubble detachment diameter and lifetime. (b) The standard deviation σ divided by the mean value for mean detachment diameter and mean lifetime versus potential at three different concentrations.

The mean values and the standard deviations σ in Fig. 7(b) are obtained by averaging over all bubbles of the experiments in Table 1 where more than three detachments occur. They are plotted as $\sigma/\overline{d}$ and $\sigma/\overline{T}$ in %, respectively. Although both the detachment diameter and the lifetime vary from bubble to bubble, the standard deviation of $\overline{T}$ is generally higher than for $\overline{d}$. This significant scatter of $\overline{T}$ already became obvious in Fig. 5a. The reason is seen in stochastic events, e.g. in the accidental pinning of the contact line of the bubble at the Pt-electrode/glass interfaces, or the adhesion of the bubble to the glass. Both events dictate a reduction in the electric current or the growth rate, which leads to longer lifetimes. The dependency of the individual bubble lifetime T on the electric current is presented in Supplementary Information†. If the adhesion is not interrupted by coalescence, the bubble evolution runs into Scenarios (2) and (3), as mentioned in Section 3.1.

3.2.5 Forces influencing the detachment of bubbles under microgravity

Figure 7 has shown that the lifetime of the bubbles at the electrode varies with potential and concentration. On one hand, this might be related to the forces which attract the bubble towards the electrode. On the other hand, the above-mentioned stochastic effects caused by contact line pinning or adhesion to the electrode/glass surface and subsequent accidental release by coalescence may play a role.

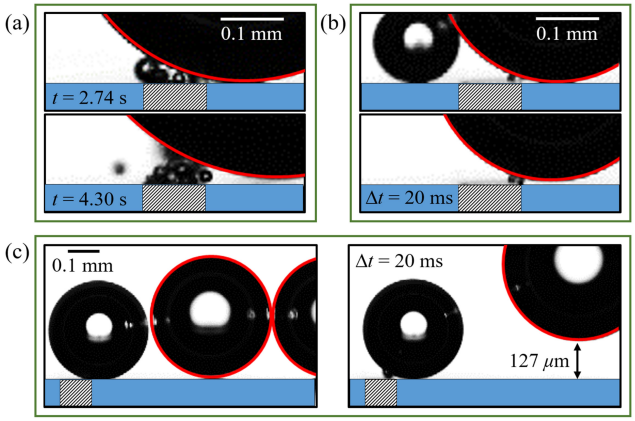

Fig. 8 (a) A bubble growing in 0.02 mol/L at -8 V at two instants of time. The first image represents the bubble adhering to the glass interface and the second one the same bubble at a later stage levitating above the surface. (b) and (c) represent two quantitatively different cases of the bubble jump above the surface caused by the bubble-bubble coalescence in 0.02 mol/L, -5 V. The two images in both (b) and (c) show the bubble immediately before and after coalescence.

Let us begin by discussing the latter issue. Once the bubble sticks additional energy is required to overcome the surface tension/adhesion forces. The bubble may detach either due to an increase in buoyancy (1g, hyper-g) or due to the coalescence-driven jump mechanism. *Jumps* of the bubbles after coalescence are frequent events, as documented by Figure 8. The first images of (a-b) show a mother bubble stuck to the electrode-glass interface while one or more smaller bubbles have been formed nearby. The second images in (a-b) depict the situation shortly after coalescence has happened. As a result, the bubble is lifted by a few micrometers. Figure 8c displays the particularly interesting case of coalescence between bubbles of a similar size: the energy that is released, transferred to the resultant bubble, is obviously enough to force both detachment under μg and to enable the bubble to jump 127 μm above the surface.

The coalescence-driven bubble detachment shown in Figure 8, is known in the literature as a self-propelled bubble removal[38,39]. The phenomenon is indebted to the excessive surface energy liberated via bubble-bubble coalescence. As two bubbles coalesce together, a deformation wave propagates. When the wave returns to the surface with enough energy to overcome the wetting forces, the bubble jumps away from the surface perpendicularly for a certain distance, governed by the released surface energy

$$\Delta E_\sigma = 2\pi\sigma(d/2)^2 - \pi\sigma(d/\sqrt[3]{4})^2\,,$$

see in detail Moreno et al.[40]. The phenomenon is widely known among studies of droplet dynamics on superhydrophobic surfaces[38,41–43] and has been discussed in detail for the gas bubbles in Moreno Soto et al.[40,44], with hydrogen bubbles first being mentioned as early as 1961[45].

The importance of the size of the two coalescing bubbles is pointed out in Moreno Soto et al.[44]. When two bubbles of a similar size coalesce, the symmetrical deformation wave causes the resultant bubble to jump. If the radii differ significantly, the symmetry of the much smaller deformation wave breaks and barely perturbs the mother bubble. The latter case is also typical of our experiments, in which we noticed numerous detachments similar to Fig. 8(b) with small jumps of a few μm because of the small size of the microbubbles coalescing with the mother bubble.

Beside coalescence, further forces may influence the bubble detachment. Similarly to terrestrial experiments, the hydrogen bubble experiences an electric force F_e (see Sect. 1). In Bashkatov et al.[6], the electric force was shown to vary non-linearly with the vertical bubble position, governing its vertical oscillations. This vertical motion of the bubble on the ground takes place in an axisymmetric electric field, while the lateral motion of the bubble away from the electrode center leads to a non-axisymmetric configuration. Nevertheless, F_e is also expected to have an influence under μg. Indeed, the experiments show at least two indications of the relevance of the electric force: (i) the bubble return events (Fig. 5a) occur more frequently at -6 V (0.02 mol/L) than at -1.5 V (0.1 mol/L). (ii) The lateral distance $\Delta\overline{X}/\overline{d}$ over which the bubble moves back to the electrode increases with the potential (Fig. 6c).

A further candidate influencing the detachment is the thermocapillary effect[7,8,30,31]. The Marangoni stress τ_M scales with the level of Joule dissipation. Thus it increases along with the potential applied and decreases with the conductivity of the electrolyte. As the bubble moves laterally away from the electrode, the Joule heating can be expected to become asymmetric, leading to an axially non-symmetric temperature distribution. The ensuing thermocapillary stress will thus also cause a sideways component of the Marangoni force to act on the bubble. In addition, residual gravitational acceleration, which cannot be completely avoided during parabolic flights, may also influence the bubble motion. In summary, the balance of the hitherto discussed three forces provides a general concept for the sideways motion and the eventual lift-off of the bubble, which still requires further investigation.

3.3 Comparison of bubble growth between micro-g, hyper-g and 1g

To highlight the differences in the formation of the above-mentioned *carpet of microbubbles* between μg and $(1...1.8)g$, a zoom into the bubble bottom during the hyper-g-phase is provided in Figure 9. Here, numerous microbubbles are visible, sandwiched between the mother bubble and the electrode, forming what we call the carpet of microbubbles. Despite the difference in atmospheric pressure and gravitational acceleration, the morphology of the carpet stays the same as on the ground[6]. This is in strong contrast to the microgravity experiments, where a carpet of microbubbles was not observed in this form. Instead, the microbubble carpet forms beside the mother bubble (cf. Fig. 8a) due to its lateral movement under microgravity.

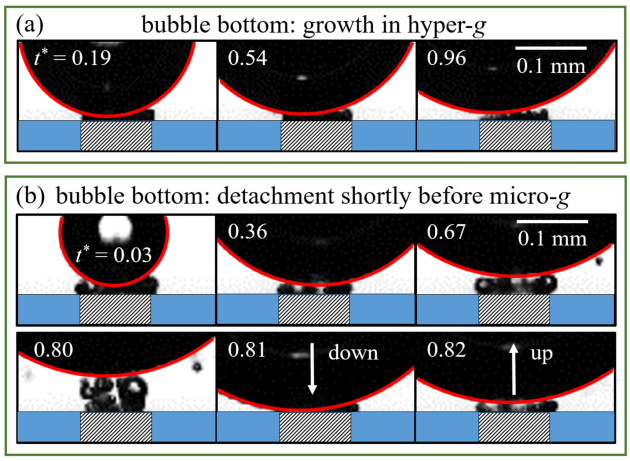

Fig. 9 Bubble evolution accompanied by the carpet of microbubbles in hyper-g (a) in 0.1 mol/L at -4 V and (b) 0.02 mol/L at -8 V. In (b) the bubble return phenomenon is additionally included in the last three images. The evolution starts in hyper-g but the bubble detaches shortly before entering micro-g zone. t^* is the dimensionless time, t/T, normalized with the bubble lifetime T.

To gain a better understanding of the role of buoyancy in the carpet formation, another example is presented on Figure 9(b) where the bubble nucleation occurred under hyper-g and the detachment shortly before entering micro-g. In this state, the bubble sits on the carpet and is able to return to the electrode several times, as shown in the last three images before the final departure. The phenomenon is a shortened version of the bubble position oscillations discussed in Bashkatov et al.[6] and is related to the non-linear variation of electric force. By contrast, a bubble that grows in the μg phase at a pitch angle close to zero, implying that the bubble stays close to the electrode, only admits a very thin carpet, which is hard to distinguish (cf. Fig. 3a at $t = 0.1$ s and 0.2 s). Thus, we can conclude that the carpet of microbubbles exists as a response to the competing forces. When the bubble is trying to leave the electrode under $(1...1.8)g$ conditions, moving away from the electrode over a $\mathcal{O}(\mu\text{m})$ distance, the electric force increases and levitates the bubble above the electrode. The gap in between enables the carpet of microbubbles to be formed.

In Figure 10 the mean electric current $\bar{I}$, obtained by averaging over time, is plotted versus electric potential. The three subfigures are dedicated to the three electrolyte concentrations studied: (i) 0.02, (ii) 0.1 and (iii) 0.5 mol/L. We see that the current grows from μg via normal-g toward hyper-g (1.5...1.8g) if the potential and concentration are fixed. We note that $\bar{I}$ under μg is smaller by a factor of at least two (2.2...3.9) than under hyper-g. As expected, at a fixed concentration $\bar{I}$ increases with the potential, further enhancing the contrast between the μg and hyper-g phase.

In Figure 11 the hydrogen production rate $\dot{V}$ is plotted versus electric potential for three electrolyte concentrations at different

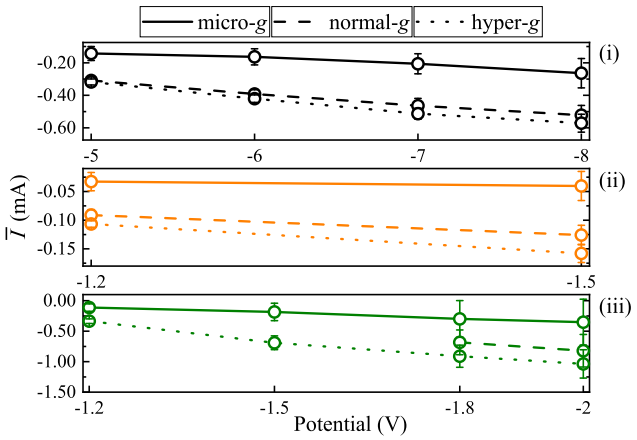

Fig. 10 Electric current averaged over time of normal-g, hyper-g and micro-g, respectively for (i) 0.02, (ii) 0.1 and (iii) 0.5 mol/L versus potential. All measurements were made during the flight and therefore under reduced atmospheric pressure ($P \sim 0.8$ atm inside the airplane).

acceleration levels. It is calculated as

$$\dot{V} = \frac{\overline{I}}{2 \cdot F} \cdot \frac{R_{H_2} \cdot T}{P},$$

where $\overline{I}$ is the time-averaged current, T is the temperature (293 K) and P is the pressure (81060 Pa) in the aircraft. Further, F and R_{gas} denote the Faraday constant (96485 C/mol) and the gas constant (8.314 $m^3 \cdot Pa/K \cdot mol$).

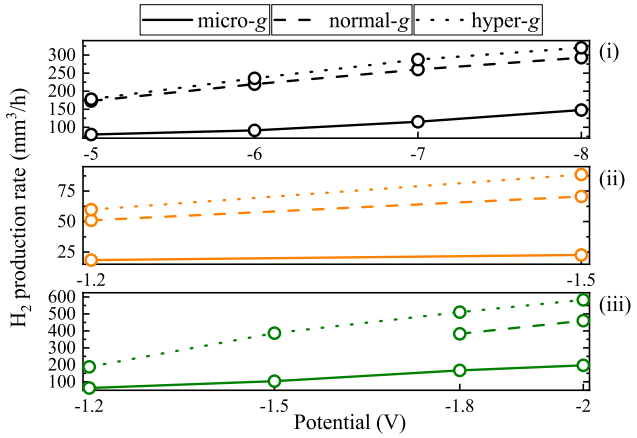

Fig. 11 Hydrogen production rate versus potential at normal-g, hyper-g and micro-g for (i) 0.02, (ii) 0.1 and (iii) 0.5 mol/L. All measurements were made during flight ($P \sim 0.8$ atm inside the airplane).

As the mean current $\overline{I}$ increases with the gravitational acceleration level (see also Fig. 10), the same is observed for the hydrogen production rate. Thus, at the same time, the Ohmic resistance reduces, which in general is beneficial for increasing the efficiency of hydrogen production.

In Figure 12 (a) the mean values of bubble detachment diameter $\overline{d}$ and lifetime $\overline{T}$ along with their standard deviation (almost negligible) are plotted versus potential for the case of hyper-g. In subfigure (b) we show the ratio of the mean values obtained in micro-g (Fig. 7) to those obtained in hyper-g, i.e. $\overline{d}^*_{\mu g/1.8g} = \overline{d}_{\mu g}/\overline{d}_{1.8g}$ and $\overline{T}^*_{\mu g/1.8g} = \overline{T}_{\mu g}/\overline{T}_{1.8g}$. We note that both $\overline{d}$ and $\overline{T}$ increase with potential and electrolyte concentration, which is similar to what is found in the terrestrial environment[31]. The effect of the reduced gravitational acceleration results in a 2.4...2.9 times higher detachment diameter and 34...78 times higher lifetime, depending on potential and concentration.

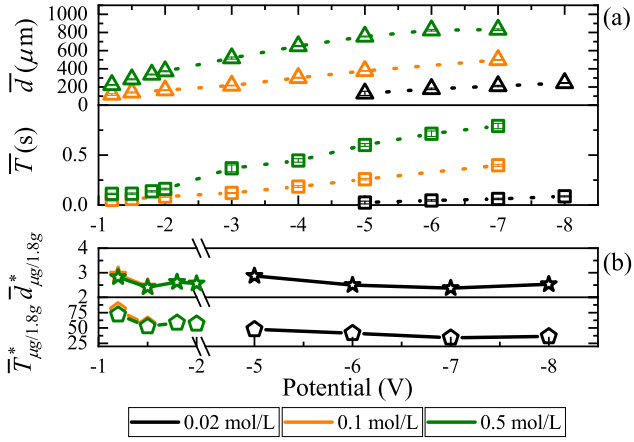

Fig. 12 (a) Bubble detachment diameter and lifetime measured in the hyper-g phases. (b) Ratio of mean detachment diameter and lifetime measured at micro-g to that measured at hyper-g versus potential at three different concentrations.

Finally, as the electric current is directly linked with the charge and hence with the hydrogen volume produced, in Figure 13 we examine the *bubble radius* $R(t)$ versus time for the different gravitational accelerations in 0.1 mol/L at -1.5 V.

The red (hyper-g), black (1g) and purple (μg) lines are obtained from the experiments on board the aircraft under reduced atmospheric pressure (~ 0.8 atm), while the dotted line refers to the experiments on the ground (1g) at 1 atm. Each line is an average over the evolution of 10 bubbles. The inset provides a zoom into the initial phase. As expected, the growth rate, influenced by the electric current, increases with increasing gravitational acceleration (cf. Fig. 10). The effect of a reduction in the atmospheric pressure becomes obvious when the dotted line (bubble evolution under 1g) is compared with the black line (1g on board the aircraft). The reduced air pressure as found in the aircraft enables a slightly faster growth.

The bubble evolution in the terrestrial environment proceeds via nucleation, growth, and detachment[3–5,27,46–49]. The growth phase can be divided in up to three stages[4], and is described by the equation

$$R(t) = \beta t^x$$

with β and x denoting the growth coefficient and the power exponent[47]. The short initial stage, lasting only for $\mathcal{O}$(ms), is governed by liquid inertia and characterized by $x = 1$[45,47,50]. Depending on whether diffusion of the dissolved hydrogen[45,47,50–52] or coalescence with smaller hydrogen bubbles[3,27,36,48,53] is the dominating growth mechanism, $x = 1/2$ or $x = 1/3$ is observed. The detachment results from either bubble unpinning processes like bubble neck-breaking of the electrode-attached bubble[4] or from losing contact with the carpet of microbubbles underneath[6]. In the case of an upward-

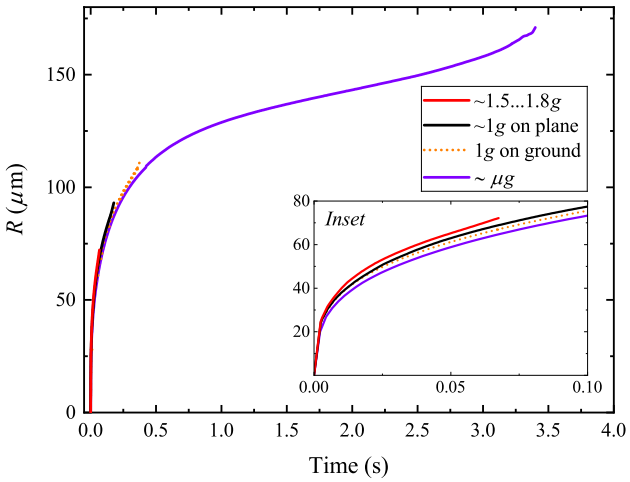

Fig. 13 Bubble evolution $R(t)$ in 0.1 mol/L at -1.5 V under different levels of gravitational acceleration and atmospheric pressures (see legend). Each line reflects the evolution averaged over 10 bubbles. The inset zooms into the initial phase.

facing/horizontal electrode without external flow, the bubble detaches perpendicular to it.

In contrast to that, the evolution under micro-g during the parabolic flights follows one of the three scenarios discussed in Sect. 3.1 and proceeds differently from that in 1g. The bubble evolution phases discussed above are summarized for both cases in Table 2.

We recall the bubble, levitating slightly above or being attached to the electrode/glass surface, may grow by both, diffusion and coalescence with the much smaller bubbles continuously nucleating at the electrode. The detachment is caused by either vertical or lateral movement (or a combination of both directions) of the bubble away from the electrode such that no further coalescence events (and growth by diffusion) are possible. The analysis of the power law in terms of the growth coefficient β and the power exponent x gives a more complex result, as both quantities vary during the bubble evolution and also with potential and concentration. Also, attached and laterally moving bubbles cause a different Ohmic resistance, resulting in different values of β and x as well. At fixed electrolyte concentration, the growth rate increases upon increasing the potential. While the growth mechanism stays similar for the low concentrations (0.02 and 0.1 mol/L), the behavior at 0.5 mol/L differs. The power coefficient might generally vary from 0.2 to 1. More details on the growth law for Scenario (1) (see Table 1) are summarized in in the Supplementary Information[†].

As the Pt microelectrodes used during the experiments were treated and cleaned in a unique way, their wettability can be assumed to be very similar. However, as the wettability might slightly modify with ongoing duration of the experiments[5,27], it is worth to take this aspect into account in future experiments.

4 Summary and conclusions

The evolution of single hydrogen bubbles at a Pt microelectrode was studied in potentiostatic experiments in an acidic electrolyte under microgravity during parabolic flights. Three characteristic scenarios of bubble evolution were found depending on the potential and electrolyte concentration: (1) - *growth and lateral detachment*, (2) - *continuous slow growth* or (3) - *initial growth and stagnation*. Contrary to expectations, Scenario (1), *lateral bubble motion*, instead of Scenario (3), *the blockage of the electrode* was found to be dominant and therefore further analyzed in detail.

As buoyancy is largely not present, detached bubbles stay close by the electrode. Driven by small horizontal components of residual gravitational acceleration, the bubbles start to slowly drift horizontally away from the electrode center. Here, due to the asymmetry of the resulting current density and the temperature distribution with respect to the electrode center, resulting horizontal components of thermocapillary and electric forces may also come into play. However, both point in opposite directions and partially cancel each other out. During the further slow lateral motion of the bubbles, reversals of the drift velocity are observed. These can clearly be correlated with coalescence events with smaller bubbles taking place prior to the reversal. As the phenomenon of a lateral shift of the center of mass during coalescence is well known, we believe the velocity reversal can mainly be attributed to the coalescence. To what extent horizontal components of thermocapillary and electric forces contribute to the phenomenon must be left for future work, which should include a detailed analysis of the momentum of the bubble-surrounding liquid (Kelvin impulse)[54]. The phenomenon was shown to be dependent on the potential applied and bears similarities with the bubble position oscillations recently reported in Bashkatov et al.[6]. The slow lateral bubble movement is believed to be responsible for the disappearance of the microbubble carpet found in standard gravity conditions, as the larger number of coalescence events with the microbubbles consumes the entire carpet, without exception.

Further noticable differences between microgravity and normal/hyper-gravity concern the averaged current $\bar{I}$, which is smaller under microgravity by a factor of more than two, a contrast which increases even further upon an increase in the potential. As a result, the rise in the bubble radius $R(t)$ proceeds more slowly than under normal or hyper-gravity.

In summary, lateral motion is an important feature of hydrogen bubble dynamics under reduced gravity. It allows enhanced mass transfer toward the electrode and continuous hydrogen production, despite Ohmic losses are larger in comparison to normal and hyper-g. The potential for bubbles to stick to the electrode or the neighboring glass surface is an undesired event leading to Scenarios (2) and (3).

Since only a very limited number of tools are available to remove the bubbles from the surface, the self-propelled coalescence-driven removal mechanism is a valuable tool for microgravity applications. Indeed, when the momentum from bubble-bubble coalescence is enough to overcome the wetting forces, the bubble jumps over remarkable distances from a few μm to more than 120 μm away from the surfaces. This is enough to transfer the resultant bubble to the bulk by other means, such as additional external fluid flow. Albeit not studied here, the results could also be useful with respect to the oxygen evolution and more generally to develop strategies for increasing the gas

		nucleation	growth	detachment
Presence in $1g$		✓	✓	✓(vertically)
Presence in micro-g for various scenarios	(i)	✓	✓	✓(laterally)
	(ii)	✓	✓(continuous growth)	none
	(iii)	✓	limited by electrode blockage	none

Table 2 Presence of the different bubble evolution phases in $1g$ and in micro-g (achieved in parabolic flights)

production rate in microgravity applications.

Conflicts of interest

There are no conflicts to declare.

Acknowledgments

This project is supported by the German Space Agency (DLR) with funds provided by the Federal Ministry of Economics and Technology (BMWi) due to an enactment of the German Bundestag under Grant No. DLR 50WM1758 (project MADAGAS) and Grant No. DLR 50WM2058 (project MADAGAS II). Furthermore, we gratefully acknowledge the support by Novespace for organizing the 34^{th} DLR Parabolic flight campaign, Dr. Christina Knapek, Ekoplasma Project, Deutsches Zentrum für Luft- und Raumfahrt e.V., Institut für Materialphysik im Weltraum, Wessling, Germany for sharing their acceleration data and by Thalheim Spezial Optik Pulsnitz (Germany) for designing a vibration-resistant microscope system.

Notes and references

1 D. Lohse, *Physical Review Fluids*, 2018, **3**, 110504.
2 S. M. H. Hashemi, P. Karnakov, P. Hadikhani, E. Chinello, S. Litvinov, C. Moser, P. Koumoutsakos and D. Psaltis, *Energy & Environmental Science*, 2019, **12**, 1592–1604.
3 X. Yang, F. Karnbach, M. Uhlemann, S. Odenbach and K. Eckert, *Langmuir*, 2015, **31**, 8184–8193.
4 A. Angulo, P. van der Linde, H. Gardeniers, M. Modestino and D. F. Rivas, *Joule*, 2020, **4**, 555–579.
5 R. Iwata, L. Zhang, K. L. Wilke, S. Gong, M. He, B. M. Gallant and E. N. Wang, *Joule*, 2021.
6 A. Bashkatov, S. S. Hossain, X. Yang, G. Mutschke and K. Eckert, *Physical Review Letters*, 2019, **123**, 214503.
7 J. Massing, G. Mutschke, D. Baczyzmalski, S. S. Hossain, X. Yang, K. Eckert and C. Cierpka, *Electrochimica Acta*, 2019, **297**, 929–940.
8 S. S. Hossain, G. Mutschke, A. Bashkatov and K. Eckert, *Electrochimica Acta*, 2020, **353**, 136461.
9 S. Ardo, D. F. Rivas, M. A. Modestino, V. S. Greiving, F. F. Abdi, E. A. Llado, V. Artero, K. Ayers, C. Battaglia, J.-P. Becker *et al.*, *Energy & Environmental Science*, 2018, **11**, 2768–2783.
10 I. Staffell, D. Scamman, A. V. Abad, P. Balcombe, P. E. Dodds, P. Ekins, N. Shah and K. R. Ward, *Energy & Environmental Science*, 2019, **12**, 463–491.
11 C. Vogt, M. Monai, G. J. Kramer and B. M. Weckhuysen, *Nature Catalysis*, 2019, **2**, 188–197.
12 P. A. Kempler, R. H. Coridan and N. S. Lewis, *Energy & Environmental Science*, 2020, **13**, 1808–1817.
13 P. A. Kempler, Z. P. Ifkovits, W. Yu, A. I. Carim and N. S. Lewis, *Energy & Environmental Science*, 2021, **14**, 414–423.
14 W. Wopersnow and C. J. Raub, *Z. Flugwiss. Weltraumforsch.*, 1978, **2**, 341–345.
15 J. Richter and H. Behret, in *Fluid Sciences and Materials Science in Space*, Springer, 1987, pp. 141–157.
16 K. Brinkert, M. H. Richter, Ö. Akay, J. Liedtke, M. Giersig, K. T. Fountaine and H.-J. Lewerenz, *Nature Communications*, 2018, **9**, 1–8.
17 A. Iwasaki, H. Kaneko, Y. Abe and M. Kamimoto, *Electrochimica Acta*, 1998, **43**, 509–514.
18 H. Matsushima, T. Nishida, Y. Konishi, Y. Fukunaka, Y. Ito and K. Kuribayashi, *Electrochimica Acta*, 2003, **48**, 4119–4125.
19 H. Matsushima, Y. Fukunaka and K. Kuribayashi, *Electrochimica Acta*, 2006, **51**, 4190–4198.
20 G. Sakuma, H. Matsushima and Y. Fukunaka, *JASMA: Journal of the Japan Society of Microgravity Application*, 2008, **25**, 517–520.
21 D. Kiuchi, H. Matsushima, Y. Fukunaka and K. Kuribayashi, *Journal of The Electrochemical Society*, 2006, **153**, E138–E143.
22 M. Sakurai, Y. Sone, T. Nishida, H. Matsushima and Y. Fukunaka, *Electrochimica Acta*, 2013, **100**, 350–357.
23 H. Kaneko, K. Tanaka, A. Iwasaki, Y. Abe, A. Negishi and M. Kamimoto, *Electrochimica Acta*, 1993, **38**, 729–733.
24 P. Mandin, Z. Derhoumi, H. Roustan and W. Rolf, *Electrochimica Acta*, 2014, **128**, 248–258.
25 V. Nefedov, V. Serebritskii, O. Ksenzhek, V. Nikitskii and M. Bocharova, *Russian Journal of Electrochemistry*, 1994, **30**, 1229–1233.
26 H. Matsushima, D. Kiuchi, Y. Fukunaka and K. Kuribayashi, *Electrochemistry Communications*, 2009, **11**, 1721–1723.
27 G. Sakuma, Y. Fukunaka and H. Matsushima, *International Journal of Hydrogen Energy*, 2014, **39**, 7638–7645.
28 J. Zhou, Y. Zhang and J. Wei, *Applied Thermal Engineering*, 2018, **132**, 450–462.
29 R. De Jonge, E. Barendrecht, L. Janssen and S. Van Stralen, *International Journal of Hydrogen Energy*, 1982, **7**, 883–894.
30 S. A. Guelcher, Y. E. Solomentsev, P. J. Sides and J. L. Anderson, *Journal of the Electrochemical Society*, 1998, **145**, 1848–1855.
31 X. Yang, D. Baczyzmalski, C. Cierpka, G. Mutschke and K. Eckert, *Physical Chemistry Chemical Physics*, 2018, **20**, 11542–11548.
32 S. Lubetkin, *Electrochimica Acta*, 2002, **48**, 357–375.
33 S. Lubetkin, *Langmuir*, 2003, **19**, 10774–10778.

34 B. J. Kirby, *Micro and Nanoscale Fluid Mechanics. Transport in Microfluidic Devices*, Cambridge University Press, 2010.

35 V. S. Craig, *Current Opinion in Colloid & Interface Science*, 2011, **16**, 597–600.

36 R. Darby and M. Haque, *Chemical Engineering Science*, 1973, **28**, 1129–1138.

37 P. Kristof and M. Pritzker, *Journal of Applied Electrochemistry*, 1997, **27**, 255–265.

38 K. Zhang, F. Liu, A. J. Williams, X. Qu, J. J. Feng and C.-H. Chen, *Physical Review Letters*, 2015, **115**, 074502.

39 J. Zhou, B. Qi, Y. Zhang, J. Wei, Y. Yang and Q. Cao, *Experimental Thermal and Fluid Science*, 2020, **112**, 109996.

40 A. Moreno Soto, *Bubbles on surfaces: Diffusive growth & electrolysis*, 2019.

41 J. B. Boreyko and C.-H. Chen, *Physical Review Letters*, 2009, **103**, 184501.

42 F.-C. Wang, F. Yang and Y.-P. Zhao, *Applied Physics Letters*, 2011, **98**, 053112.

43 K. M. Wisdom, J. A. Watson, X. Qu, F. Liu, G. S. Watson and C.-H. Chen, *Proceedings of the National Academy of Sciences*, 2013, **110**, 7992–7997.

44 Á. M. Soto, T. Maddalena, A. Fraters, D. Van Der Meer and D. Lohse, *Journal of Fluid Mechanics*, 2018, **846**, 143–165.

45 D. E. Westerheide and J. Westwater, *AIChE Journal*, 1961, **7**, 357–362.

46 C. Sillen, E. Barendrecht, L. Janssen and S. Van Stralen, in *Hydrogen as an Energy Vector*, Springer, 1980, pp. 328–348.

47 N. Brandon and G. Kelsall, *Journal of Applied Electrochemistry*, 1985, **15**, 475–484.

48 D. Fernandez, P. Maurer, M. Martine, J. Coey and M. E. Möbius, *Langmuir*, 2014, **30**, 13065–13074.

49 P. van der Linde, P. Peñas-López, Á. M. Soto, D. van der Meer, D. Lohse, H. Gardeniers and D. F. Rivas, *Energy & Environmental Science*, 2018, **11**, 3452–3462.

50 J. Glas and J. Westwater, *International Journal of Heat and Mass Transfer*, 1964, **7**, 1427–1443.

51 P. S. Epstein and M. S. Plesset, *The Journal of Chemical Physics*, 1950, **18**, 1505–1509.

52 L. Scriven, *Chemical Engineering Science*, 1959, **10**, 1–13.

53 H. Verhaart, R. De Jonge and S. Van Stralen, *International Journal of Heat and Mass Transfer*, 1980, **23**, 293–299.

54 J. R. Blake, D. M. Leppinen and Q. Wang, *Interface Focus*, 2015, **5**, 20150017.